Research Square

Preprints are preliminary reports that have not undergone peer review.
They should not be considered conclusive, used to inform clinical practice,
or referenced by the media as validated information.

DKIST unveils MHD-predicted sub-50 km photospheric vortices

Santiago Vargas-Dominguez

svargasd@unal.edu.co

Universidad Nacional de Colombia

Oscar Andrés Calvo-Rebellon

Universidad Nacional de Colombia

Juan Sebastián Castellanos-Durán

Max Planck Institute for Solar System Research

Michiel van Noort

Max Planck Institute for Solar System Research

Friedrich Woeger

National Solar Observatory

Daniel Alberto Rodriguez-Torres

Universidad Nacional de Colombia

Cristian Giovanny Bernal

Universidad Nacional de Colombia

Research Article

Keywords: Velocity Fields, Photosphere, Granulation, Magnetic fields, Photosphere

Posted Date: September 11th, 2026

DOI: https://doi.org/10.21203/rs.3.rs-10990993/v1

License: This work is licensed under a Creative Commons Attribution 4.0 International License.
Read Full License

Additional Declarations: No competing interests reported.

DKIST unveils MHD-predicted sub-50 km photospheric vortices

S. Vargas Domínguez[1] · O. A. Calvo Rebellon[1] · J. S. Castellanos Durán[2] · M. van Noort[2] · F. Wöger[3] · D. A. Rodríguez Torres[1] · C. G. Bernal[4]

© **The author(s)** ●●●●

Abstract Solar vortices are rotating plasma structures that play a key role in the transport of energy and magnetic helicity from the photosphere to the chromosphere and corona. While numerical simulations predict the existence of small-scale photospheric vortices with diameters of 50–100 km, no direct observational evidence has been reported to date, primarily due to the limited spatial resolution of previous instrumentation. Here, we analyze high-resolution observations taken by the 4-meter Daniel K. Inouye Solar Telescope (DKIST) at 416 nm with a 12.3 km spatial resolution. Using Fourier local correlation tracking and the swirling strength criterion (λ_{ci}), we identify 201 vortex detections over a sequence of 143 reconstructed frames (≈3.2 min) in a field-of-view of 4.92×4.13 Mm, covering a photospheric plage region with pore-like magnetic concentrations. The detected vortices have a median equivalent diameter of 38.6 km (mean 39.5 ± 3.3 km), with virtually all detections below 50 km, therefore in the sub-granular regime predicted by MHD simulations, but never previously observed. The median swirling period $\tau_{ci} = 37.3$ s satisfies the $\tau_{ci} < 100$ s criterion established by MURaM simulations. No statistically significant preference for prograde (53.7%) over retrograde (46.3%) rotation is found, consistent with the negligible role of the Coriolis force at sub-granular scales. These results demonstrate the unique capability of DKIST to resolve the photospheric convective

✉ S. Vargas Domínguez
svargasd@unal.edu.co

[1] Universidad Nacional de Colombia, Observatorio Astronómico Nacional, Bogotá, Colombia

[2] Max-Planck-Institut für Sonnensystemforschung, 37077 Göttingen, Germany

[4] Universidad Nacional de Colombia, Departamento de Física, Bogotá, Colombia

[3] National Solar Observatory, 3665 Discovery Drive, Boulder, CO 80303, USA

vortex population predicted by state-of-the-art magnetoconvection simulations, opening a new observational window on small-scale solar convective dynamics.

Keywords: Velocity Fields: Photosphere – Granulation – Magnetic fields: Photosphere

1. Introduction

Vortical motions in the solar atmosphere have been identified across a wide range of spatial and temporal scales, from large-scale vortices of several megameters (e.g., Su et al. (2012); Wedemeyer-Böhm et al. (2012)) to small photospheric swirls of a few hundred kilometers (Bonet et al. 2008; Wedemeyer-Böhm and Rouppe van der Voort 2009). These rotating plasma structures are thought to play a fundamental role in the transport of energy and magnetic helicity along flux tubes connecting the photosphere to the upper solar atmosphere, potentially contributing to chromospheric and coronal heating (Wedemeyer-Böhm et al. 2012; Shelyag et al. 2011; Tziotziou et al. 2023).

State-of-the-art magnetoconvection simulations with the MURaM code (Vögler et al. 2005) have made specific predictions about photospheric vortices at the smallest scales. Moll, Cameron, and Schüssler (2011) demonstrated that the intergranular network harbors a rich population of vortex tubes with diameters of 50–100 km and lifetimes of tens to hundreds of seconds. Yadav, Cameron, and Solanki (2021), simulating a unipolar plage region with a mean field of 200 G at 10 km grid resolution, found that sub-granular vortices are denser and hotter than their surroundings in the chromosphere, and that strong electric current sheets at their interfacesprovide an efficient mechanism for chromospheric heating. Those authors explicitly noted that these structures had never been observed directly due to the insufficient spatial resolution of existing instrumentation.

Prior observational studies have been fundamentally limited by angular resolution. Bonet et al. (2008) identified vortices of 0.5–1″ (360–720 km) with the Swedish Solar Telescope (SST). Balmaceda et al. (2010) and Vargas Domínguez et al. (2015) tracked magnetic bright points dragged into photospheric vortex centers using SST G-band and Ca II H imagery. Vargas Domínguez et al. (2011) provided the first statistical characterization of LCT-derived vortex-like motions in a quiet-Sun region. The SUNRISE balloon-borne observatory pushed the frontier to structures of ≈150 km at 300 nm (Yelles Chaouche et al. 2020), extending the turbulent power spectrum by more than a factor of two in wavenumber space. Kitiashvili et al. (2012) showed with NST/BBSO observations at 77 km resolution that agreement with simulated kinetic energy spectra requires an effective resolution of at least 150 km, still insufficient to resolve the sub-granular vortex population.

The Daniel K. Inouye Solar Telescope (DKIST; Rimmele et al. 2020), with its 4-meter primary mirror, represents a four-fold improvement in aperture over SUNRISE (Korpi-Lagg et al. 2025) and more than an order of magnitude over Hinode/SOT (Ichimoto et al. 2008). In its highest-resolution configuration, DKIST achieves a plate scale of ≈6 km pixel^{-1} at visible wavelengths, placing

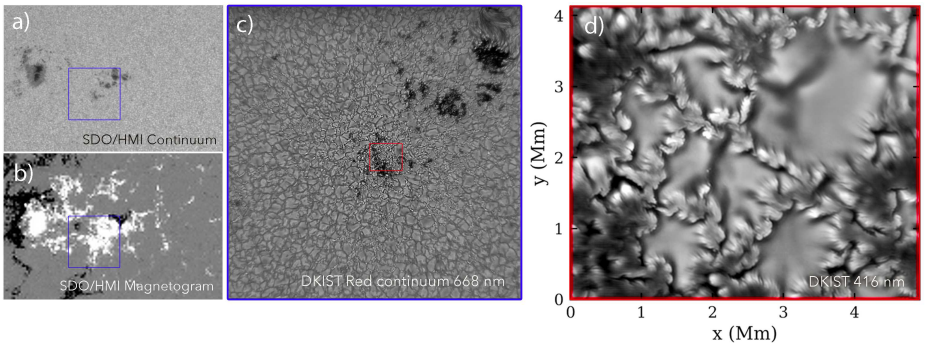


Figure 1. Multi-wavelength context of the observed solar region on 2025 April 14 at 21:33 UT, centred near heliographic position ($\mu = -162\farcs2, +168\farcs5$) in the north-western quadrant. (a) SDO/HMI continuum intensity at 617 nm showing the large-scale photospheric structure; the blue box indicates the field of view of the DKIST/VBI red-continuum image shown in panel (c). (b) SDO/HMI line-of-sight magnetogram saturated at ±500 G; the blue box is the same as in panel (a), marking the DKIST/VBI field of view; the target region is associated with a small unipolar flux concentration adjacent to a solar pore, with no evidence of strong flux emergence during the observing window. (c) DKIST/VBI red-continuum image at 668 nm showing the photospheric granulation and the solar pore at high spatial resolution; the red box indicates the field of view of the DKIST fast-camera sequence shown in panel (d). (d) DKIST fast-camera image at 416 nm (Ca II H wing, bandpass 0.5 nm FWHM) used for the vortex detection analysis; the field of view covers 4.92 × 4.13 Mm after reconstruction with the multi-frame blind deconvolution (MFBD) technique and removal of the instrumental padding. Solar north is up and east is to the left in all panels.

the sub-granular vortex scales predicted by MURaM within observational reach for the first time; in the same DKIST observing sequence analyzed here, Kuridze et al. (2026) visually identified prominent vortex-like structures.

In this work, we present the first detection and statistical characterization of sub-granular vortices in direct photospheric observations using DKIST data at 416 nm. Section 2 describes the observations and context data. Section 3 presents the detection and tracking pipeline. Section 5 reports the results. Section 6 discusses implications. Section 7 summarizes our conclusions.

2. Observations

The observations were obtained on 2025 April 14 starting at 21:33:37 UT with DKIST at Haleakalā, Hawaii. The primary dataset consists of high-cadence intensity images at 416 nm acquired with a diagnostic fast-camera setup (MPS FastCam[1]; Jai Spark SP12000CXP4) temporarily installed in front of the Visible Spectro-Polarimeter (ViSP) spectrograph entry slit, in collaboration with the Max-Planck-Institut für Sonnensystemforschung (MPS), Göttingen. The bandpass filter had a full width at half maximum (FWHM) of 0.5 nm centered at 416 nm (Alluxa ultra-narrow bandpass, OD6). Images were acquired at 740 Hz. Multi-frame blind deconvolution (MFBD; Löfdahl 2002) reconstructions were

[1] dkist.virtualsolar.org/vanNoortfastcam/

computed from overlapping sets of 2000 raw frames offset by 1000 frames, yielding a pseudo-cadence of $\Delta t = 1000/740 \approx 1.35\,\mathrm{s}$. The total sequence covers $\approx 3.2\,\mathrm{min}$ ($N = 143$ frames). The plate scale is $\Delta x = 0.00848''\,\mathrm{pixel}^{-1}$ (i.e., $6.15\,\mathrm{km\,pixel}^{-1}$ at disk center).

The observed target is a photospheric plage region with pore-like magnetic flux concentration at helioprojective coordinates $(-162'', +168'')$. The multi-scale observational context is shown in Fig. 1. The large-scale magnetic environment was characterized with the Helioseismic and Magnetic Imager (HMI; Scherrer et al. 2012) aboard SDO. Co-temporal HMI continuum images and line-of-sight magnetograms ($0.5''\,\mathrm{pixel}^{-1}$, cadence 45 s) confirm that the DKIST field samples a unipolar plage region of negative polarity, with line-of-sight flux densities of -50 to $-400\,\mathrm{G}$, directly comparable to the 200 G mean-field simulation of Yadav, Cameron, and Solanki (2021). High-resolution photospheric context was obtained simultaneously with the Visible Broadband Imager (VBI) in the red continuum 668 nm ($\approx 50 \times 23''$). The VBI red-continuum frames reveal dark pore-like structures of equivalent diameter 1500–3400 km in the immediate surroundings of the 416 nm FOV.

The MFBD reconstruction pads the image borders with a constant value of 562.26 counts. This region was identified by detecting rows and columns with an intensity standard deviation below 5 counts; a 10-pixel safety margin was then applied. Each frame was cropped to rows 49–849, columns 50–721 in the raw FITS array (671×800 pixels) and then aligned with solar North up and East to the left. The resulting analysis array is 800×671 pixels, corresponding to a physical FOV of $4.92 \times 4.13\,\mathrm{Mm}$ (solar X $\times$ Y) $= 20.3\,\mathrm{Mm}^2$. Intensity stability across the full sequence is excellent, with rms $= 2.35$ counts over a mean of ≈ 556 counts. The methodology for detecting vortices, which employs Fourier local correlation tracking (FLCT; Fisher and Welsch 2008) and the swirling strength criterion (λ_{ci}; Zhou et al. 1999; Haller 2005), in the methods Section 3.

3. Methods

3.1. Velocity field estimation

Horizontal velocity fields were computed from consecutive frame pairs using Fourier local correlation tracking (FLCT; Fisher and Welsch 2008). Each frame was normalized to its spatial mean prior to tracking. The algorithm used a Gaussian apodization window of 20 pixels ($\approx 123\,\mathrm{km}$) and a post-tracking 5-pixel spatial smoothing filter. The displacement field $\boldsymbol{u} = (u_x, u_y)$ was converted to physical velocity via

$$\boldsymbol{v} = \frac{\Delta x}{\Delta t}\,\boldsymbol{u}, \tag{1}$$

yielding horizontal velocities in the range -9 to $+10\,\mathrm{px\,frame}^{-1}$ (≈ -45 to $+50\,\mathrm{km\,s}^{-1}$), consistent with published granular flow velocities in plage regions (Vargas Domínguez et al. 2011). The time-averaged horizontal velocity field over the full 3.2-min sequence is shown in Fig. 2a.

Table 1. Vortex detection pipeline parameters.

Parameter	Value
LCT window	20 px (≈123 km)
LCT sigma	5 px
Velocity smoothing	5 px
Plate scale	$6.15\,\mathrm{km\,px^{-1}}$
Cadence	1.35 s
λ_{ci} threshold	99th percentile ($= 0.232\,\mathrm{s^{-1}}$)
Min. τ_{ci}	$\approx 27\,\mathrm{s} = 2\pi/\lambda_{\mathrm{ci}}^{\mathrm{thr}}$
Min. region size	28 px ($r_{\mathrm{eq}} \gtrsim 18\,\mathrm{km}$)
Morphol. closing	disk $r = 2$ px
Max. drift	60 km
Max. radius ratio	< 2.5

3.2. Vortex detection

Vortices were identified using the swirling strength criterion (λ_{ci}; Zhou et al. 1999; Haller 2005), which detects genuinely rotating flow independently of local shear. For the velocity gradient tensor

$$\mathbf{J} = \begin{pmatrix} \partial v_x/\partial x & \partial v_x/\partial y \\ \partial v_y/\partial x & \partial v_y/\partial y \end{pmatrix}, \tag{2}$$

the discriminant is $\Delta = (\mathrm{tr}\,\mathbf{J})^2 - 4\,\det\mathbf{J}$. When $\Delta < 0$ the eigenvalues are complex conjugates and

$$\lambda_{\mathrm{ci}} = \tfrac{1}{2}\sqrt{-\Delta} \tag{3}$$

quantifies the local swirling rate ($\mathrm{rad\,s^{-1}}$), with swirling period $\tau_{\mathrm{ci}} = 2\pi/\lambda_{\mathrm{ci}}$.

We emphasize that λ_{ci} (and hence τ_{ci}) is an instantaneous diagnostic of the local velocity-gradient tensor, computed independently for each frame pair. It quantifies the instantaneous rate of rotation of the flow, analogous to an instantaneous angular velocity, and does not require the underlying rotational pattern to persist for a full period $2\pi/\tau_{\mathrm{ci}} = 37.3\,\mathrm{s}$. A vortex detected in a single frame with $\tau_{\mathrm{ci}} = 37.3\,\mathrm{s}$ indicates that the local flow is rotating at a rate corresponding to one revolution per 37.3 s at that instant, independently of how long the structure itself survives (see Sect. 4 for further discussion of tracked lifetimes).

The rotation sense (CCW or CW) follows from the sign of the vorticity

$$\omega = \partial v_y/\partial x - \partial v_x/\partial y. \tag{4}$$

The detection threshold is the 99th percentile of the global λ_{ci} distribution over all 142 frame pairs and all pixels in the field, giving $\lambda_{\mathrm{ci}}^{\mathrm{thr}} = 0.232\,\mathrm{s^{-1}}$ and a minimum detectable swirling period $\tau_{\mathrm{ci}}^{\mathrm{min}} \approx 27\,\mathrm{s}$, well within the $\tau_{\mathrm{ci}} < 100\,\mathrm{s}$ criterion of Yadav, Cameron, and Solanki (2021).

3.3. Vortex characterization and tracking

Connected regions above threshold were extracted after morphological closing with a 2-pixel disk and removal of objects smaller than 28 pixels ($r_{\rm eq} \lesssim 18$ km). For each gion we compute the equivalent radius $r_{\rm eq} = \sqrt{A/\pi}\,\Delta x$, circularity $C = 4\pi A/P^2$, mean swirling strength $\langle\lambda_{\rm ci}\rangle$, swirling period $\tau_{\rm ci} = 2\pi/\langle\lambda_{\rm ci}\rangle$, and rotation sense from $\mathrm{sgn}(\langle\omega\rangle)$. Vortices were tracked across consecutive frames with a nearest-neighbor algorithm imposing a maximum centroid drift of 60 km and a maximum equivalent-radius ratio of 2.5. Tracks shorter than two frames were discarded. Representative examples of individually resolved CCW and CW vortices are shown in Fig. 2b–c. All pipeline parameters are summarized in Table 1.

4. Overview of vortex detection

A summary of the results of vortex detection is provided in Tab. 2

5. Results

The pipeline detects 201 vortex instances across 142 frame pairs, with a mean rate of 1.42 frame^{-1} and a spatial density of 0.070 Mm^{-2} over the 20.3 Mm^2 FOV. The peak simultaneous count is 7 vortices at frame 26 ($t = 35.1$ s; Fig. 3, panel (a)). The detection rate reflects the stringency of the 99th percentile threshold, which retains only the most intensely rotating structures.

The median equivalent diameter is 38.6 km (mean 39.5 ± 3.3 km; Fig. 3, panel (e)). Virtually all 201 detections lie below 50 km, and can be considered in the sub-granular regime. All detections fall well below the 150 km resolution limit of SUNRISE/IMaX (Yelles Chaouche et al. 2020), confirming a population inaccessible to all prior solar telescopes.

The median swirling period is $\tau_{\rm ci} = 37.3$ s (Fig. 3, panel (f)), well below the $\tau_{\rm ci} < 100$ s criterion of Yadav, Cameron, and Solanki (2021), confirming dynamic consistency with the simulated sub-granular vortex population. Of the 201 detections, 108 (53.7%) are CCW and 93 (46.3%) are CW. A two-sided binomial test gives $p = 0.29$, which confirms no statistically significant asymmetry (Fig. 3, panel (c)). This result is consistent with the dominance of convective driving over the Coriolis force at sub-granular scales.

The centroid map accumulated over the full sequence (Fig. 3, panel (c)) shows a tendency toward intergranular lane regions, consistent with Moll, Cameron, and Schüssler (2011); Yadav, Cameron, and Solanki (2021). The temporal tracking yields 190 resolved tracks with a median lifetime of 1.35 s and a maximum of 4.05 s (Fig. 3, panel (g)).

6. Discussion

The vortices detected in this work match key predictions of Yadav, Cameron, and Solanki (2021) for a plage region. The median diameter of 38.6 km lies

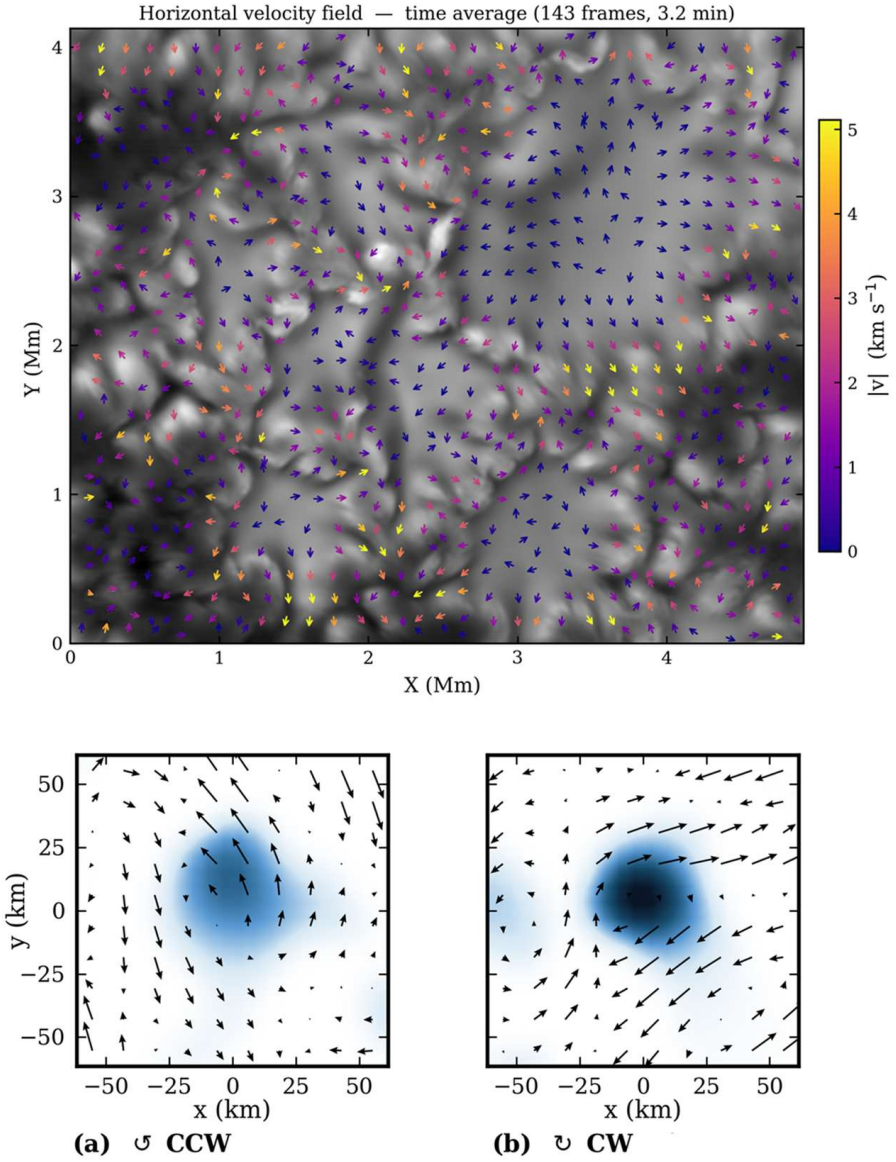


Figure 2. Horizontal velocity field derived from local correlation tracking (LCT) applied to the full DKIST 416 nm sequence (143 frames, cadence 1.35 s). *Top:* Time-averaged horizontal velocity map over the full FOV (4.92 × 4.13 Mm). Arrows indicate the direction and relative magnitude of proper motions, and the background image shows the mean intensity. The typical flow pattern associated with granular convection cells is clearly visible, with diverging outflows at granule centres and converging inflows at intergranular lanes. *Bottom left* and *bottom right:* Close-up views of two representative detected vortices, one counter-clockwise (CCW) and one clockwise (CW), respectively. The background image in each panel shows the local swirling-strength map $\lambda_{\rm ci}$, and the arrows show the instantaneous horizontal velocity field. The rotational sense of each vortex is clearly reflected in the curling pattern of the velocity arrows.

Table 2. Summary of vortex detection results.

Quantity	Value
Observing date	2025 April 14
Wavelength	416 nm
Plate scale	6.15 km px^{-1}
Cadence	1.35 s
Total frames	143
Duration	191.9 s (3.2 min)
FOV	4.92×4.13 Mm (20.3 Mm^2)
Total detections	201
Mean per frame	1.42
Max. per frame	7 (frame 26)
Spatial density	0.070 Mm^{-2}
Median diameter	38.6 km
Mean $\pm$ std diam.	(39.5 ± 3.3) km
Max. diameter	55.9 km
Fraction < 50 km	>99%
Fraction < 150 km	100%
$\lambda_{\rm ci}^{\rm thr}$	0.232 s^{-1}
Min. $\tau_{\rm ci}$	$\approx$27 s
Median $\tau_{\rm ci}$	37.3 s
CCW	53.7% (108 events)
CW	46.3% (93 events)
Binomial p	0.29
Tracked vortices	190
Median lifetime	1.35 s
Maximum lifetime	4.05 s

just below the lower end of the predicted 50–100 km range, consistent with the stringent 99th percentile threshold selecting compact and intense vortex cores. The median $\tau_{\rm ci} = 37.3$ s lies well within the $\tau_{\rm ci} < 100$ s criterion of Yadav, Cameron, and Solanki (2021). The co-temporal HMI magnetogram confirms a unipolar plage of negative polarity with -50 to -400 G and, therefore, can be directly compared to the 200 G simulation of Yadav, Cameron, and Solanki (2021). The detected density of 0.070 Mm^{-2} is approximately one order of magnitude below the $\sim$1 Mm^{-2} predicted by Moll, Cameron, and Schüssler (2011). We attribute this to the imposed percentile threshold, which suppresses sensitivity for the detection of faint vortices. Compared with prior observations, the vortices reported here are one order of magnitude smaller in diameter than those of Bonet et al. (2008) and Balmaceda et al. (2010), and nearly a factor of twenty smaller than those of Vargas Domínguez et al. (2011). This directly reflects the fourfold improvement in resolution afforded by DKIST.

Unlike the larger ($\geq$150 km) vortices reported in previous studies, for which lifetimes of tens to hundreds of seconds have been measured, the structures

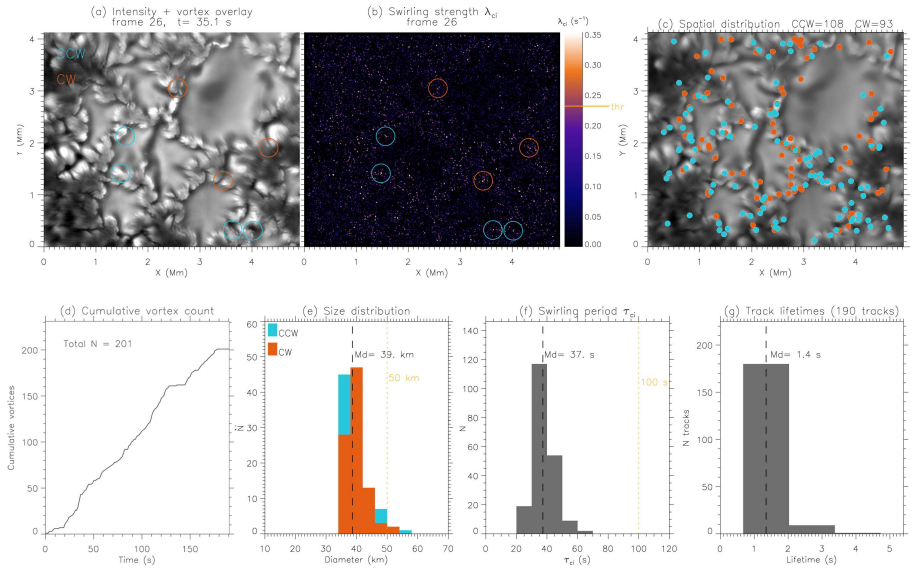


Figure 3. Summary of the vortex detection pipeline results on the DKIST 416 nm time series (143 frames, 3.2 min, FOV = 4.92 × 4.13 Mm). *(a)* Intensity image at frame 26 (t = 35.1 s, peak count N = 7) with detected vortices overlaid as circles (cyan: CCW; orange: CW). *(b)* Swirling-strength map $\lambda_{\rm ci}$ for the same frame. The yellow line in the color bar marks the detection threshold ($\lambda_{\rm ci}^{\rm thr} = 0.232\,{\rm s}^{-1}$, 99th percentile); vortex circles follow the same colour convention as panel (a). *(c)* Spatial distribution of all 201 vortex centroids accumulated over the full sequence, overlaid on the time-averaged intensity image (CCW: cyan; CW: orange). *(d)* Number of detections per frame versus time. *(e)* Equivalent diameter distribution separated by rotation sense (CCW: cyan; CW: orange). Black dashed line: median diameter ($\tilde{d} = 38.6$ km); orange dotted line: 50 km lower bound of sub-granular vortices in MURaM simulations (Yadav, Cameron, and Solanki 2021). *(f)* Distribution of swirling periods $\tau_{\rm ci} = 2\pi/\lambda_{\rm ci}$. Black dashed line: median ($\tilde{\tau}_{\rm ci} = 37.3$ s); orange dotted line: $\tau_{\rm ci} = 100$ s criterion of Yadav, Cameron, and Solanki (2021). *(g)* Track lifetime distribution for 190 resolved vortex tracks (black dashed: median 1.35 s; maximum: 4.05 s).

identified here have median diameters of only 38.6 km. A simple scaling estimate, lifetime $\approx r_{\rm eq}/vflow$, using $r_{\rm eq} \lesssim 18$ km and the intergranular flow speeds of 1–5 km s^{-1} measured here (Fig. 2a), yields characteristic lifetimes of order 4–20 s, comparable to our measured values and to the cadence of the observations. Also, the swirling period is an instantaneous diagnostic of the local rotation rate and is not expected to coincide with the tracked lifetime (see Methods 3.2). We therefore interpret the short tracked lifetimes not as an artifact of the detection, but as a natural consequence of resolving a smaller-scale, faster-evolving vortex population than has not been accessible to previous instrumentation. In addition, visual inspection of the full-cadence movie reveals larger, more slowly rotating structures with longer apparent lifetimes at intergranular junctions, which correspond to vortices with λ_{ci} below our 99th-percentile threshold and are not included in the statistics presented here. A dedicated lower-threshold analysis targeting this larger-covered-area, longer-lived population is left for future work.

The time-averaged horizontal velocity field (Fig. 2a) reveals the granular flow pattern with typical outflows of 1–2 km s^{-1} from granule centers and faster flows (> 3 km s^{-1}) concentrated along the intergranular lanes where vortex activity is also enhanced. This is consistent with the picture of vortices being generated at the intersection of diverging granular flows (Moll, Cameron, and Schüssler 2011). We note that the horizontal velocity field used in this work is derived from FLCT, and that inferred vortex properties can depend on the velocity-estimation method, detection criterion, spatial resolution, and magnetic configuration (e.g., Turkay et al. 2026; Koll Pistarini et al. 2026). In this context, the stringent 99th-percentile λ_{ci} threshold adopted here preferentially selects the strongest, most compact, and smallest-scale swirling signatures in the FLCT-derived velocity field.

7. Conclusions

We have presented the first direct observational detection of sub-granular vortices in the solar photosphere using 416 nm DKIST imagery. Applying Fourier LCT and the swirling strength criterion to a 3.2-min sequence of 143 MFBD-reconstructed frames over a 4.92×4.13 Mm plage FOV, we detect 201 vortex instances. Our main conclusions are summarized as follows (see also Tab. 2):

1. The median equivalent diameter is 38.6 km (mean 39.5 ± 3.3 km). Virtually all 201 detections lie below 50 km, and all lie well below the 150 km resolution limit of SUNRISE, placing them within the 20–55 km size range predicted by MURaM simulations (Moll, Cameron, and Schüssler 2011; Yadav, Cameron, and Solanki 2021) and previously inaccessible to direct observation.
2. The median swirling period $\tau_{\rm ci} = 37.3$ s satisfies the $\tau_{\rm ci} < 100$ s criterion of MURaM simulations (Yadav, Cameron, and Solanki 2021).
3. The spatial density of 0.070 Mm^{-2} is a conservative lower bound set by the 99th percentile threshold.
4. We found no statistically significant rotation-sense asymmetry (CCW: 53.7%, CW: 46.3%, $p = 0.29$), consistent with the dominance of convection over the Coriolis force at these scales.
5. Temporal tracking yields 190 resolved tracks with a median lifetime of 1.35 s and a maximum of 4.05 s; given the observational cadence, these values represent lower bounds on the true vortex lifetimes (see Section 6).
6. The time-averaged horizontal velocity field resolves the granular convective pattern with typical flows of 1–5 km s^{-1}, providing direct evidence that the detected vortices are embedded in the intergranular convective network.
7. These results demonstrate the unique resolving power of DKIST for solar convective dynamics and open a direct observational window on the sub-granular vortex population long predicted by magnetoconvection simulations.

Future work will search for chromospheric counterparts of the detected vortices in the co-spatial Hα 656 nm and Ca II IR observations. MURaM simulations predict that photospheric vortices of this scale drive torsional Alfvén waves that

produce observable brightenings and swirling motions in chromospheric diagnostics (Yadav, Cameron, and Solanki 2021), providing a direct observational test of the vortex-driven heating mechanism inferred from numerical models.

Acknowledgements The authors thank the DKIST operations team at the National Solar Observatory for support during the observations. The data were obtained as part of a diagnostic test conducted in collaboration between NSO and MPS, Göttingen. DKIST is a facility of the National Science Foundation operated by NSO under a cooperative agreement with AURA, Inc. The HMI data are courtesy of NASA/SDO and the HMI science team. The research was sponsored by the DynaSun project and has thus received funding under the Horizon Europe programme of the European Union under grant agreement (no. 101131534). Views and opinions expressed are however those of the author(s) only and do not necessarily reflect those of the European Union and therefore the European Union cannot be held responsible for them."

References

Balmaceda, L., Vargas Domínguez, S., Palacios, J., Cabello, I., Domingo, V.: 2010, Evidence of small-scale magnetic concentrations dragged by vortex motion of solar photospheric plasma. *Astron. Astrophys.* **513**, L6. DOI.

Bonet, J.A., Márquez, I., Sánchez Almeida, J., Cabello, I., Domingo, V.: 2008, Convectively Driven Vortex Flows in the Sun. *Astrophys. J. Lett.* **687**, L131. DOI.

Fisher, G.H., Welsch, B.T.: 2008, FLCT: A Fast, Efficient Method for Performing Local Correlation Tracking. *ASP Conf. Ser.* **383**, 373.

Haller, G.: 2005, An objective definition of a vortex. *J. Fluid Mech.* **525**, 1. DOI.

Ichimoto, K., Lites, B., Elmore, D., Suematsu, Y., Tsuneta, S., Katsukawa, Y., Shimizu, T., Shine, R., Tarbell, T., Title, A., Kiyohara, J., Shinoda, K., Card, G., Lecinski, A., Streander, K., Nakagiri, M., Miyashita, M., Noguchi, M., Hoffmann, C., Cruz, T.: 2008, Polarization Calibration of the Solar Optical Telescope onboard Hinode. *Sol. Phys.* **249**, 233. DOI. ADS.

Kitiashvili, I.N., Kosovichev, A.G., Mansour, N.N., Wray, A.A.: 2012, Turbulent Convection in the Sun: Comparing Realistic Simulations and High-resolution Observations. *Astrophys. J. Lett.* **751**, L21. DOI.

Koll Pistarini, M., Khomenko, E., Felipe, T., Modestov, M.: 2026, Solar vortex detection methods in MHD simulations: Impact of magnetic field and spatial resolution. *Astron. Astrophys.* **711**, A265. DOI. ADS.

Korpi-Lagg, A., Gandorfer, A., Solanki, S.K., et al.: 2025, Sunrise III: Overview of Observatory and Instruments. *Solar Physics* **300**, 75. DOI.

Kuridze, D., Wöger, F., van Noort, M., Rempel, M., Cameron, R., Rimmele, T., Solanki, S.K., Jaeggli, S.A., Tritschler, A., Uitenbroek, H., Przybylski, D., Boboltz, D.A.: 2026, Ubiquitous Kelvin–Helmholtz instabilities driving plasma mixing on the Sun. *Nature* **656**, 595. DOI. https://doi.org/10.1038/s41586-026-10871-3.

Löfdahl, M.G.: 2002, Multi-frame blind deconvolution with linear equality constraints. *Proc. SPIE* **4792**, 146. DOI.

Moll, R., Cameron, R.H., Schüssler, M.: 2011, Vortices in simulations of solar surface convection. *Astron. Astrophys.* **533**, A126. DOI.

Rimmele, T.R., Warner, M., Keil, S.L., et al.: 2020, The Daniel K. Inouye Solar Telescope – Observatory Overview. *Sol. Phys.* **295**, 172. DOI.

Scherrer, P.H., Schou, J., Bush, R.I., Kosovichev, A.G., Bogart, R.S., Hoeksema, J.T., Liu, Y., Duvall, T.L., Zhao, J., Title, A.M., Schrijver, C.J., Tarbell, T.D., Tomczyk, S., et al.: 2012, The Helioseismic and Magnetic Imager (HMI) Investigation for the Solar Dynamics Observatory (SDO). *Solar Physics* **275**, 207. DOI.

Shelyag, S., Keys, P., Mathioudakis, M., Keenan, F.P.: 2011, Vorticity in the solar photosphere. *Astron. Astrophys.* **526**, A5. DOI.

Su, Y., Wang, T., Veronig, A., Temmer, M., Gan, W.: 2012, SOLAR MAGNETIZED "TORNADOES:" RELATION TO FILAMENTS. *The Astrophysical Journal Letters* **756**, L41. DOI. https://doi.org/10.1088/2041-8205/756/2/L41.

Turkay, S.S., Scullion, E., Botha, G.J.J., Rees-Crockford, T.: 2026, The Reliability of Local Correlation Tracking for Inferring Photospheric Intensity Vortices. *Astrophys. J.* **999**, 58. DOI. ADS.

Tziotziou, K., Tsiropoula, G., Kontogiannis, I., Scullion, E., Doyle, J.G.: 2023, Vortex Motions in the Solar Atmosphere: Definition, Theory, Observations, and Modelling. *Space Sci. Rev.* **219**, 1. DOI.

Vargas Domínguez, S., Palacios, J., Balmaceda, L., Cabello, I., Domingo, V.: 2011, Spatial distribution and statistical properties of small-scale convective vortex-like motions in a quiet-Sun region. *Mon. Not. R. Astron. Soc.* **416**, 148. DOI.

Vargas Domínguez, S., Palacios, J., Balmaceda, L., et al.: 2015, Evolution of Small-Scale Magnetic Elements in the Vicinity of Granular-Sized Swirl Convective Motions. *Solar Physics* **290**, 301. DOI.

Vögler, A., Shelyag, S., Schüssler, M., et al.: 2005, Simulations of magneto-convection in the solar photosphere. Equations, methods, and results of the MURaM code. *Astron. Astrophys.* **429**, 335. DOI.

Wedemeyer-Böhm, S., Rouppe van der Voort, L.: 2009, Small-scale swirl events in the quiet Sun chromosphere. *Astron. Astrophys.* **507**, L9. DOI.

Wedemeyer-Böhm, S., Scullion, E., Steiner, O., et al.: 2012, Magnetic tornadoes as energy channels into the solar corona. *Nature* **486**, 505. DOI.

Yadav, N., Cameron, R.H., Solanki, S.K.: 2021, Vortices in the photosphere and chromosphere of a simulated unipolar region. *Astron. Astrophys.* **645**, A3. DOI.

Yelles Chaouche, L., Cameron, R.H., Solanki, S.K., et al.: 2020, Power spectra of solar velocity and intensity from SUNRISE and MURaM simulations. *Astron. Astrophys.* **644**, A44. DOI.

Zhou, J., Adrian, R.J., Balachandar, S., Kendall, T.M.: 1999, Mechanisms for generating coherent packets of hairpin vortices in channel flow. *J. Fluid Mech.* **387**, 353. DOI.